Taylor & Francis
Taylor & Francis Group

Synchrotron Techniques Applied to Ferroelectrics: Some Representative Cases

L. Fuentes-Montero,[1] M. E. Montero-Cabrera,[1] L. Calzada,[2] M. Pérez De la Rosa,[3] O. Raymond,[4] R. Font,[4] M. García,[5] A. Mehta,[6] M. Torres,[2] and L. Fuentes[1],*

[1]Centro de Investigación en Materiales Avanzados, Chihuahua, México
[2]Instituto de Ciencia de Materiales de Madrid, Cantoblanco, Madrid, España
[3]University of Texas at El Paso, El Paso, TX, USA
[4]Centro de Ciencias de la Materia Condensada, Ensenada, Baja California, México
[5]Instituto de Investigación en Materiales, UNAM, Ciudad México, México
[6]Stanford Synchrotron Radiation Laboratory, Menlo Park, CA, USA

ABSTRACT

A panoramic view of synchrotron radiation techniques applied to ferroelectric materials is given. Powder diffraction is applied to analyze the cubic-symmetry break-down in $PbFe_{0.5}Nb_{0.5}O_3$. Slight peaks' splitting reveals the considered phase to be rhombohedral. Grazing incidence scattering is used in a comparative study of $PbTiO_3$ nano-dots on $SrTiO_3$ substrate and a Pt layer. Phase identification, texture assessment and crystallite size characterization are performed. The *Anaelu* software for two-dimensional diffraction analysis is presented. Local ordering in multiferroic $Bi_6Ti_3Fe_2O_{18}$ is determined by means of extended x-ray absorption fine structure. The iron cations' tendency to occupy the centered perovskite layer of the unit cell is established.

Keywords: synchrotron radiation, ferroelectric, multiferroic, Rietveld, grazing incidence, EXAFS

INTRODUCTION

Presently, synchrotrons have become relatively accessible to materials scientists. In the particular field of ferroelectric and multiferroic materials, problems like crystal symmetry, local- versus global- ordering and nano-systems'

characterization are of primary importance. Precisely for the solution of the mentioned problems, different synchrotron radiation tools are highly effective. The objective of the present paper is to divulge some case-studies of synchrotron structure analyses, referred to different challenges and techniques. Selected materials represent current areas of interest at international level and were obtained by means of a collaborative work among different groups in Mexico and in Spain. The synchrotron radiation experiments were performed at different beamlines of the Stanford Synchrotron Radiation Laboratory.

POWDER DIFFRACTION: THE $PbFe_{0.5}Nb_{0.5}O_3$ CRYSTAL SYMMETRY

Paradoxes regarding the crystal symmetry of perovskites and perovskite-related electroceramics are relatively frequent. The case of pseudo-cubic $PbFe_{0.5}Nb_{0.5}O_3$ may be considered as representative. Starting from the original cubic representation given by Agranovskaya [1], different authors have proposed rhombohedral [2] and monoclinic [3, 4] symmetries. Experimental evidences in favor of one or other hypothesis have been subtle in all published discussions. Even the cubic-rhombohedral difference in room-temperature $PbFe_{0.5}Nb_{0.5}O_3$ refers to a deviation of the order of $0.01°$ in the inter-axial angles (relative to the ideally cubic square angles). In this scenario, our group has decided to contribute an independent investigation of the considered phase symmetry, making use of the high-resolution capabilities of the powder diffractometer at the Stanford Synchrotron Radiation Laboratory (SSRL).

$PbFe_{0.5}Nb_{0.5}O_3$ was synthesized by solid state reaction, according to the description given in [5]. Conventional x-ray diffraction demonstrated the single-phase nature of the investigated material.

The synchrotron radiation diffraction data were collected at SSRL beamline 2–1. All the diffraction patterns were obtained at room temperature, under N_2 flux, using zero-background sample holders. Experiments' wavelengths were calibrated by means of a LaB_6 standard. First, a 10 keV X-rays diffraction pattern was collected in the $15° < 2\theta < 140°$ range using a step $\Delta(2\theta) = 0.005°$, wavelength $\lambda = 1.24036$ Å. Afterwards, to observe in full detail the reflections associated with relatively large reciprocal space vectors, a wide scan with 12 KeV photons ($\lambda = 1.03265$ Å) was realized.

Figure 1 shows in a resumed form the results of all the performed measurements.

Patterns' interpretation was performed by application of software *Full-prof* [6]. Rhombohedral (space group R3m) and monoclinic (Cm) models were tested. Qualitatively, all the peaks in the experimental pattern were explained with the rhombohedral model. Quantitatively, monoclinic symmetry did not lead to better calculated-observed agreement indicators. The final obtained reliability factors, identical for both models, were $R_p = 9.8$, $\chi^2 = 2.53$. Choosing
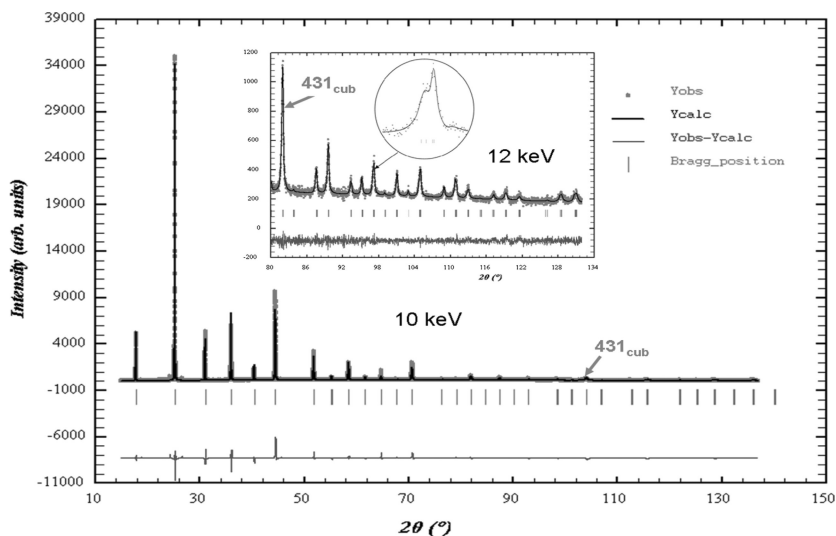
Figure 1. Synchrotron radiation diffraction patterns of $PbFe_{0.5}Nb_{0.5}O_3$. The large plot (10 keV) corresponds to $\lambda = 1.24036$ Å. The small pattern (12 keV) was measured with $\lambda = 1.03265$ Å. The arrows in both patterns point to the peak 4, 3, 1 (cubic indexes). The circular zoom in the 12 KeV diffractogram shows a typical splitting and its rhombohedral modeling. (See Color Plate XVI)

the simplest model that satisfies sufficiency, it is concluded that the performed experiment tends to confirm the rhombohedral symmetry of $PbFe_{0.5}Nb_{0.5}O_3$. Table 1 shows the investigated phase refined lattice parameters.

Refinement of atomic positions is reported in Table 2, referred to hexagonal axes. Figure 2 shows the investigated crystal unit cell. Fe and Nb atoms were assumed to share randomly their positions. Isotropic temperature factors are included, except for Fe/Nb. These atoms' temperature factors showed a tendency to negative values.

The partial conclusion of this section is that synchrotron radiation powder diffraction reveals extremely subtle deviations from cubic (in general high)

Table 1
$PbFe_{0.5}Nb_{0.5}O_3$ lattice parameters. Space group R3m

Hexagonal axes	Rhombohedral axes
a = 5.6740(1) Å	a = 4.0125(1) Å
c = 6.9511(3) Å	$\alpha = 89.99(1)°$

Table 2
Atomic parameters for $PbFe_{0.5}Nb_{0.5}O_3$. Hexagonal axes

| Atom	x	y	z	B isotropic
Pb	0.0000	0.0000	0.0000	1.74(5)
Fe/Nb	0.0000	0.0000	0.5033(7)	—
O	0.1744(5)	0.8256(5)	0.8256(7)	0.15(5)

symmetry. $PbFe_{0.5}Nb_{0.5}O_3$ (obtained as described in [5]) exhibits rhombohedral symmetry.

GRAZING INCIDENCE SCATTERING: THIN LAYERS AND NANO-DOTS

We illustrate the characterization of nanometric systems by means of grazing incidence scattering (GIS) and two-dimensional (2D) detection of diffracted radiation at beam line 11-3 at SSRL. The materials selected for a comparative study were: A) nanometric $PbTiO_3$ dots on a $SrTiO_3$ substrate; B) a thin Pt layer (to be used as substrate). Figure 3 shows the considered experimental facility. Some characteristic parameters of the experiment were: $\lambda = 0.97354$ Å, sample-detector distance $= 180$ mm, 2D-detector diameter $= 345$ mm, incidence angle $= 0.5°$, screen pixel dimensions $= 0.1$ mm. Table 3 resumes crystallographic data of the phases forming both samples. Figure 4 shows the indexed two-dimensional diffraction patterns corresponding to the mentioned samples.
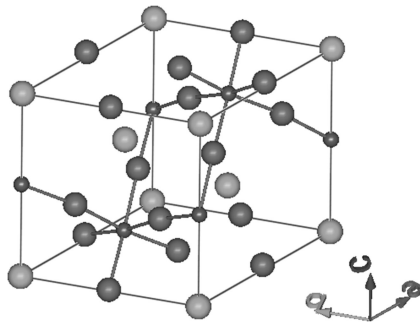
Figure 2. $PbFe_{0.5}Nb_{0.5}O_3$ crystal structure (hexagonal representation). Atoms in the corners are Pb, smallest ones are Fe/Nb. Fe/Nb – O bonds are drawn. (See Color Plate XVII)
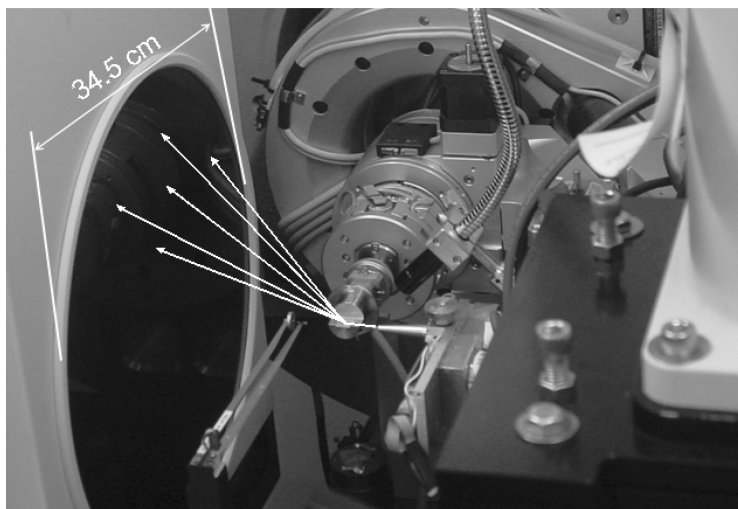
Figure 3. Grazing incidence x ray scattering at beamline 11-3, SSRL.

To convert coordinates on the screen into crystal interplanar distances, a calibration experiment with a LaB_6 polycrystalline pattern was performed. Figure 5 [7] shows the Debye rings produced by the LaB_6 sample.

Figure 6 illustrates in detail the interpretation of some representative Debye ring sectors and diffuse spots in the diffraction pattern of sample A. The image shows the working screen of program *Anaelu* [8] during modeling of the diffraction signals associated with $SrTiO_3$ planes of the form $\{1, 2, 1\}$. The fields of the screen show numerical data and geometric conditions used to simulate the diffraction events. The large circle at the left represents the stereographic projection of low-indexes poles and the circle at the right is the prediction of diffraction spots on the 2D detector under the represented conditions. Coincidence of symmetry and interplanar distances justify the $\{1, 2, 1\}$ identification and allow crystal orientation determination.

Table 3
Crystallographic data of investigated phases

	Sample A		Sample B
	SrTiO3	PbTiO3	Pt
Space group	P 4/m −3 2/m	P 4 m m	F 4/m −3 2/m
Lattice parameters (Å)	$a = 3.900$	$a = 3.8966$	$a = 3.9231$
		$c = 4.1494$	
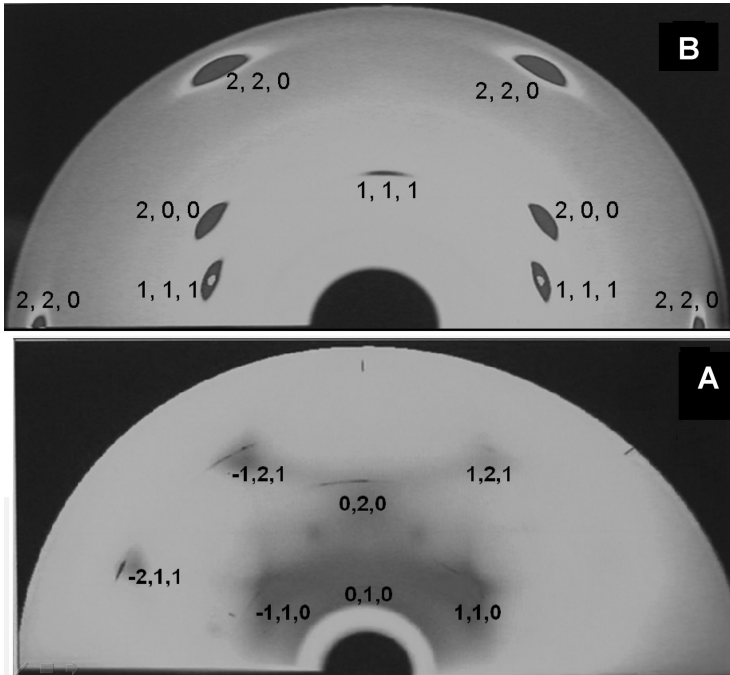
Figure 4. 2D diffraction patterns from (A) PbTiO$_3$ dots on SrTiO$_3$ and (B) Pt layer. (See Color Plate XVIII)

Observing in detail the diffracted intensity distribution, it is seen that the high-intensity zones show a complex structure, composed by a sharp ring sector and a diffuse maximum centered on a smaller dispersion angle. The zoom in Fig. 6 shows one such "doublet." The ring sectors are produced by SrTiO$_3$ crystals that form the substrate. As the ring sectors are sharp, SrTiO$_3$ crystals are large (equal or greater than one micrometer). The presence and length of the observed rings imply that the crystallites in the sample form a sharp so-called "cube texture" [9, 10], with an orientation distribution width of about 10°. The diffuse spots that appear in smaller angles are due to crystals with larger lattice parameters, namely PbTiO$_3$. The width of the PbTiO$_3$ diffraction spots leads for this phase to a crystal size of the order of some tens nm and their location (close to SrTiO$_3$ signals) is a result of the epitaxial PbTiO$_3$-SrTiO$_3$ relationship.

The high-intensity peaks in sample B 2D-diffraction pattern correspond to planes of the forms {1, 2, 1}, {0, 2, 0}, {0, 1, 0} and {1, 1, 0}. Peaks with mixed parity in the corresponding Miller indexes are extinguished. Pt has a FCC symmetry. The angular coordinates of the observed diffraction maxima,
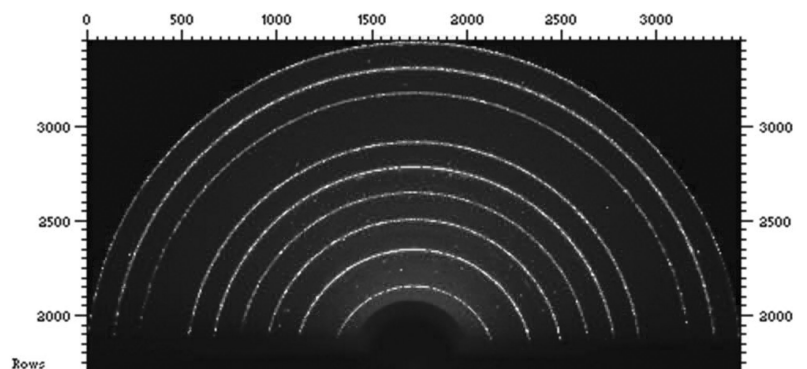
Figure 5. Diffraction rings from a LaB$_6$ sample Quantitative patterns' processing was made by the programs *Fit2d* [7] and *Anaelu* [8]. (See Color Plate XIX)
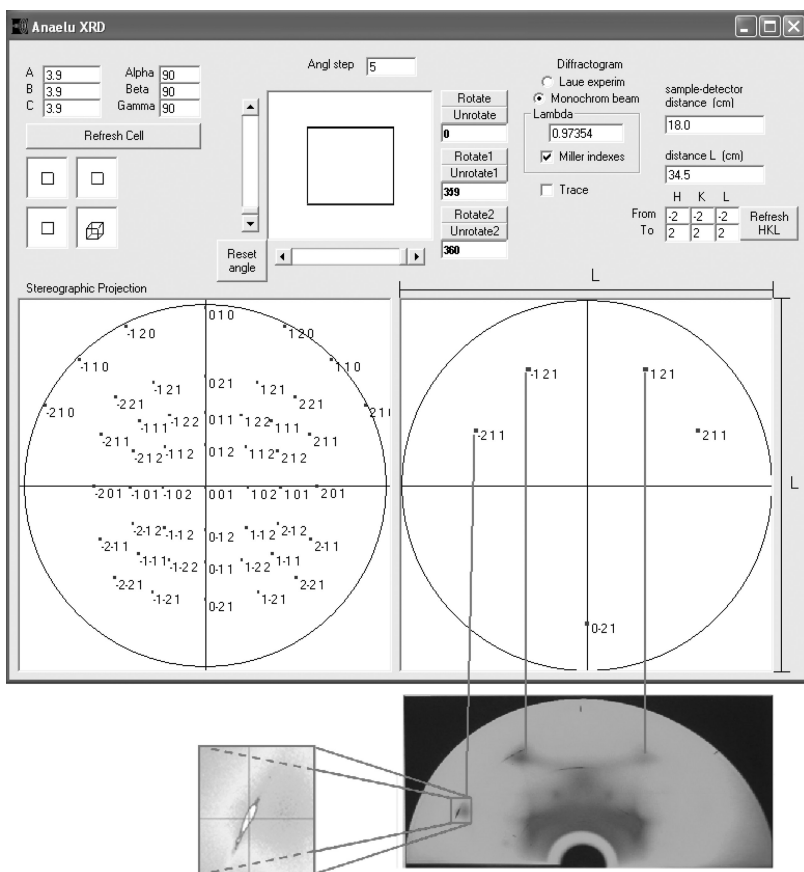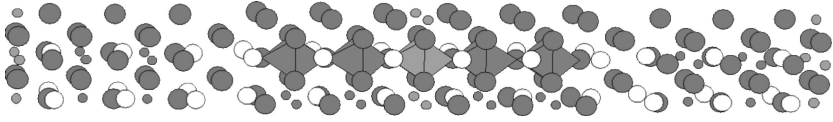

Figure 6. Sample A pattern processing via *Anaelu* software.

Figure 7. The crystal structure of $Bi_6Ti_3Fe_2O_{18}$ [ref 12]. Space group: Fmm2. Spheres: large red → O; small blue/orange → Ti/Fe; large white → Bi. a = 49.342 Å; b = 5.4655 Å; c = 5.4967 Å. Polar axis c points roughly outwards from the figure. (See Color Plate XX)

as well as their definiteness, indicate a sharp "Goss texture" [10] for the Pt sample.

The partial conclusion of the present section is that 2D-GIS reveals itself as a powerful tool for analyzing micro- and nano-metric crystal systems, providing phase identification and information about crystal perfection and orientation distribution.

EXTENDED X-RAY ABSORPTION FINE STRUCTURE

Extended X-Ray Absorption Fine Structure (EXAFS) has become a useful tool for investigating short range order in crystals and molecular interactions. EX-AFS analysis of $Bi_6Ti_3Fe_2O_{18}$ Aurivillius ceramic was performed to elucidate the local environment of Fe cations in this interesting multiferroic material. Sample was obtained by molten salts synthesis, according to the description given by García-Guaderrama et al [11]. The structure obtained by synchrotron radiation diffraction and reported in the cited reference is shown in Fig. 7. $Bi_6Ti_3Fe_2O_{18}$ crystals show a layered structure, with five perovskite octahedra "sandwiched" between bismuth oxide sheets. Small (Ti/Fe) cations occupy virtually the centers of the shown perovskite octahedra. Diffraction data suggest that Fe cations show a tendency to be located at the central octahedra, far from the Bi-oxide layers. In this context, the information obtainable by means EXAFS is highly valuable.

EXAFS spectra of $Bi_6Ti_3Fe_2O_{18}$ at 10, 30, 50, 75, 100 y 298 K were measured. Fe K absorption edge spectra (about 7112 eV) were obtained at SSRL beamline 2–3 using a Lytle fluorescence detector, at the mentioned temperatures. Raw data were processed with *SixPACK* package [12]. In the edge zone the energy intervals were $\Delta E = 0.35$ eV. After 7114 eV, in the EXAFS zone, energy intervals corresponded to $\Delta k = 0.04$ Å^{-1}. Spectra were measured up to $k = 11.7$ Å^{-1}. Figure 8 shows the amplitudes of the Fourier transform spectra $\chi(R)$ for all temperatures. This figure is related with the atomic radial distribution, centered at the x-ray absorbing atom (Fe) and somewhat shifted to the left. The near neighborhood of a Fe core atom is represented in Fig. 9.
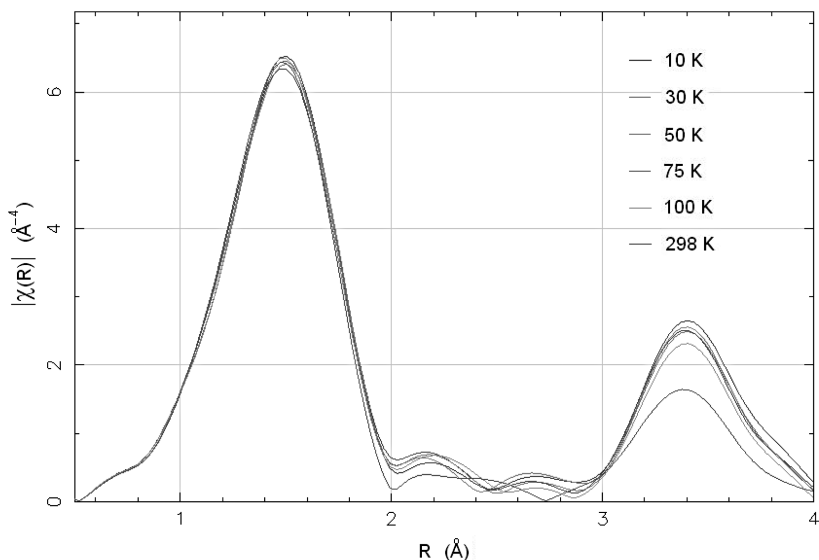
Figure 8. Fourier transforms of all spectra. (See Color Plate XXI)

The first maxima of the $\chi(R)$ spectra occur at R $\approx$ 1.5 Å. They correspond (with a left shift of $\sim$ 0.4 Å) to the first Fe-O interatomic distances around the Fe core. These peaks are the superposition of signals associated with the various distances in the first Fe-O coordination shells (Fe-O^A, Fe-O^B) along the crystal volume. Partly due to disorder, partly due to practical limitations, the present EXAFS experiment did not resolve individual distances. In the broad temperature interval from 10 to 298 K the considered maximum appears almost unaltered.
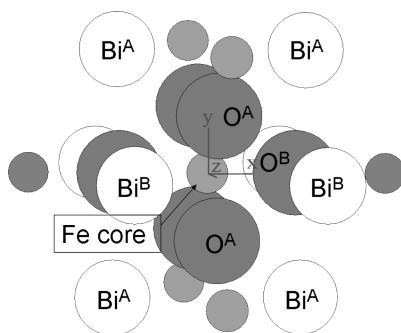
Figure 9. Closest neighbors to a Fe atom in $Bi_6Ti_3Fe_2O_{18}$. (See Color Plate XXII)

The second maxima of the $\chi(R)$ spectra characterize the different Fe-Bi bonds. Interestingly, the effect of temperature is now significant. The 298 K second peak shows less intensity than the others. It is also somewhat broader. The origin of this feature is related with high values of Debye-Waller (DW) factors, as will be considered below.

EXAFS spectra were quantitatively processed using *SixPACK* interface for *IFFEFIT* [12]. X-ray absorption was modeled by *FEFF6* [13], introducing in subroutine *ATOMS* the structure obtained by XRD. The distances among the Fe (core) and surrounding atoms were modeled. This includes Fe-bismuth, Fe-octahedral oxygen and Fe-closest Ti and Fe, in all possible positions. Six different configurations for two Fe atoms in the 5 perovskite layers were tried. Representing Ti as T and Fe as F, these configurations are: TTFFT, TTFTF, TTTFF, TFTTF, TFTFT and FTTTF. Fe core was selected, when possible, the closest to the center. For configurations TTFTF and TTFFT, when Fe cation is in the center, there are only three equations for fitting the Fe-Bi distance. For the rest of configurations there are six equations (one for each Bi). Only single scattering paths were considered. For the configurations TTFTF and TTFFT, 8 parameters were adjusted in the harmonic model and 14 parameters in the anharmonic. For configurations with Fe core farther from the cell center, 14 parameters were fitted in the harmonic model. The anharmonic model is impossible to be fitted, because there are more parameters than the number of independent points.

All configurations were processed for the six temperatures. Reduced $\Delta\chi^2$ values of less than 100 were obtained for configurations TTFFT and TTFTF at all temperatures. This range of $\Delta\chi^2$ values is not rare in EXAFS. Values of cation distances (R), Debye-Waller factors (σ^2) and anharmonic parameters (σ^3), corresponding to T = 298K, are shown in Table 4. Figure 10 shows observed and calculated $\chi(R)$ for the TTFFT configuration.

Figure 11 presents the trend of DW factors for Fe core - Bi distances, as obtained in the fitting for centered configurations at all temperatures.

DW factors (σ^2) and anharmonic terms (σ^3) are consistently small for interactions of the type Fe-O^B and Fe-Bi^B, that take place in the (xz) plane of the unit cell. Reasonably, these small DW factors are mostly thermo-vibrational in nature. A harmonic-vibrational model [14], applied to the DW results in the TTFFT configuration (for T = 10 and 298 K) is congruent with the consideration that Fe-Bi^B bonds are weaker than Fe-O^B, as is the case. The virtual absence of a static contribution to the DW factor associated with atoms in the xz plane is an indicator of a correlation among the static displacements of the atoms in that plane [15].

The observed large DW factors associated to the remaining atoms are not surprising. They were expected in view of the aspect of the 298 K Fe-Bi peak in the $\chi(R)$ plot (Fig. 8). Low amplitude peaks appear as a consequence of large disorders and anharmonic vibrations that give rise to low-k contributions in the $\chi(k)$ spectrum [16].
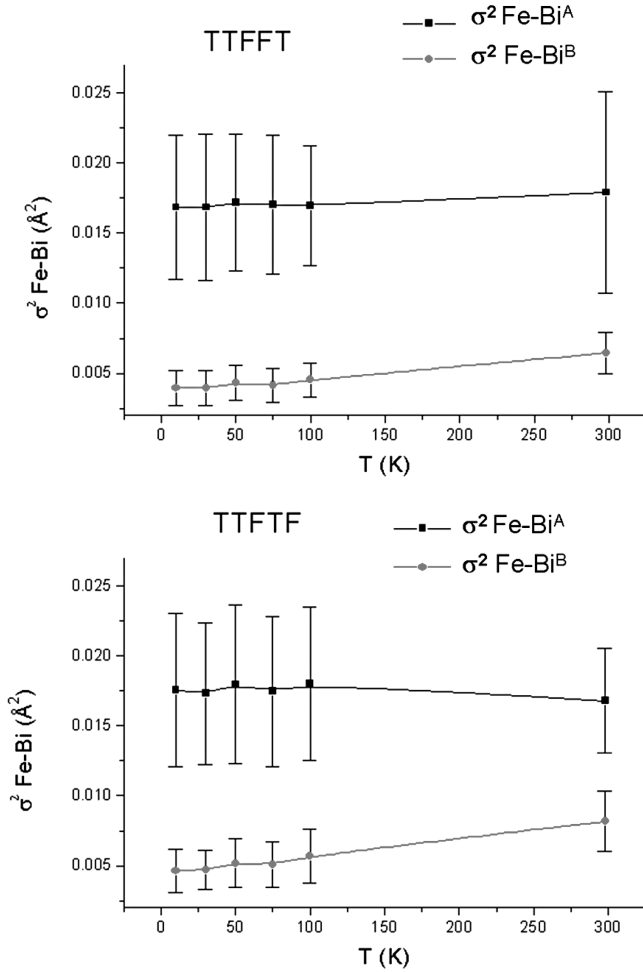
Table 4

EXAFS parameters for pairs of atoms obtained after fitting for centered configurations and T=298 K. *R* in % represents the goodness of the fitting in the R space

T = 298 K		TTFFT (R = 1.2%)	TTFTF (R = 1.5%)
Fe-O^A XRD=1.94 (Å)	R (Å)	1.84 (4)	1.85 (5)
	σ^2(Å^2)	0.017 (2)	0.021 (3)
	σ^3(Å^3)	−0.003 (1)	−0.003 (2)
Fe-O^B XRD=1.97 (Å)	R (Å)	1.97 (3)	1.96 (4)
	σ^2(Å^2)	0.006 (1)	0.005 (1)
	σ^3(Å^3)	0.0003 (3)	0.00002 (2)
Fe-Bi^A XRD=3.456 (Å)	R (Å)	3.449 (3)	3.457 (6)
	σ^2(Å^2)	0.018 (7)	0.017 (4)
	σ^3(Å^3)	0.015 (2)	0.015 (1)
Fe-Bi^B XRD=3.65 (Å)	R (Å)	3.54 (5)	3.67 (6)
	σ^2(Å^2)	0.006 (1)	0.008 (2)
	σ^3(Å^3)	0.0003 (3)	0.002 (1)

For configurations with Fe farther from the center of the cell, in the frame of the harmonic model, reduced $\Delta\chi^2$ values are greater than 200. In some configurations uncertainties of Debye Waller factors diverge. This is a result of the asymmetry of the configuration, which severely affects the fitting. As general balance of the performed calculations, the central Fe model leads to an acceptable agreement among observed and calculated spectra. All other models
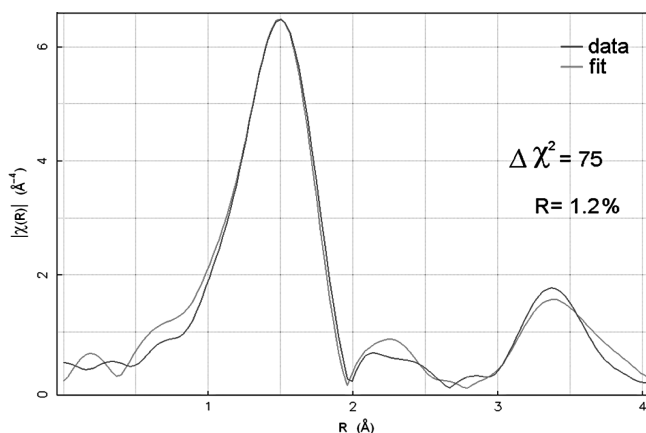
Figure 10. EXAFS function χ(R) obtained at T = 298 K and fitting for configuration TTFFT. (See Color Plate XXIII)

Figure 11. Debye-Waller factors of (Fe_{core}-Bi) pairs in perovskite layers, obtained by fitting spectra for all temperatures. TTFFT and TTFTF configurations. (See Color Plate XXIV)

lead to unacceptable observed-calculated relationships. This global result is the EXAFS argument that supports the central Fe-model.

REFERENCES

1. A. I. Agranovskaya, Izvestiya Akademii Nauk SSSR, *Seriya Fizicheskaya* **24**, 1275 (1960).
2. S. A. Ivanov, R. Tellgren, H. Rundlof, N. W. Thomas, and S. Ananta, *J. Phys. Condensed Matter* **12**, 2393 (2000).
3. N. Lampis, P. Sciau, and A. Geddo Lehmann, *J. Phys.: Condensed Matter* **11**, 3489 (1999).
4. V. Bonny, M. Bonin, P. Sciau, K. Schenk, and G. Chapuis, *Solid State Comm.* **102**, 347 (1997).
5. O. Raymond, R. Font, N. Suárez, J. Portelles, and M. Siqueiros, *Ferroelectrics* **294**, 141 (2003).
6. J. Rodríguez-Carvajal, http://www.ill.fr/dif/Soft/fp/php/downloads.html http://biosync.rcsb.org/ssrl/BL11-3.html
7. A. Hammersley: http://www.esrf.fr/computing/scientific/FIT2D/.
8. L. Fuentes-Montero and L. Fuentes, http://www.cimav.edu.mx/ie/investiga/sw/index.php
9. W. Kraus and G. Nolze, http://ccp14.minerals.csiro.au/ccp/webmirrors/powdcell/a_v/v_1/powder/e_cell.html/
10. H. R. Wenk and P. Van Houttte, *Reports on Progress in Physics* **67**, 1367 (2004).
11. M. García-Guaderrama, L. Fuentes-Montero, A. Rodriguez, and L. Fuentes, *Integrated Ferroelectrics* **83**, 41 (2006).
12. S. Webb, http://www-ssrl.slac.stanford.edu/~swebb/sixpack.htm
13. M. Newville, *J. Synchrotron Rad.* **8**, 322 (2001).
14. S. I. Zabinsky, J. J. Rehr, A. Ankudinov, R. C. Albers, and M. J. Eller, *Phys. Rev.* **B52**, 2995 (1995).
15. B. K. Teo, EXAFS, Basic Principles and Data Analysis Springer, Berlin, (1986).
16. J. J. Rehr and R. C. Albers, *Review of Modern Physics* **73**, 621 (2000).